

# Energetic analysis of the rhodopsin–G-protein complex links the $\alpha 5$ helix to GDP release

Nathan S Alexander<sup>1,4</sup>, Anita M Preininger<sup>2,4</sup>, Ali I Kaya<sup>2</sup>, Richard A Stein<sup>3</sup>, Heidi E Hamm<sup>2</sup> & Jens Meiler<sup>1,2</sup>

We present a model of interaction of  $G_i$  protein with the activated receptor ( $R^*$ ) rhodopsin, which pinpoints energetic contributions to activation and reconciles the  $\beta_2$  adrenergic receptor– $G_s$  crystal structure with new and previously published experimental data. *In silico* analysis demonstrated energetic changes when the  $G\alpha$  C-terminal helix ( $\alpha 5$ ) interacts with the  $R^*$  cytoplasmic pocket, thus leading to displacement of the helical domain and GDP release. The model features a less dramatic domain opening compared with the crystal structure. The  $\alpha 5$  helix undergoes a  $63^\circ$  rotation, accompanied by a  $5.7\text{-\AA}$  translation, that reorganizes interfaces between  $\alpha 5$  and  $\alpha 1$  helices and between  $\alpha 5$  and  $\beta 6$ – $\alpha 5$ . Changes in the  $\beta 6$ – $\alpha 5$  loop displace  $\alpha G$ . All of these movements lead to opening of the GDP-binding pocket. The model creates a roadmap for experimental studies of receptor-mediated G-protein activation.

G protein-coupled receptors catalyze GDP release on cognate G proteins through a mechanism that is not fully elucidated; however, studies released in the past several years have greatly accelerated understanding of this process. Previously, numerous structural and functional studies demonstrated the key roles of regions such as the C terminus and the  $\alpha 4$ – $\beta 6$  loop of  $G\alpha$  in receptor-mediated G-protein activation<sup>1–7</sup>. However, it was not until the crystal structure of the  $\beta_2$  adrenergic receptor ( $\beta_2AR$ )– $G_s$  complex was determined in 2011 (ref. 7) that the extent of these G protein–receptor interactions could be fully appreciated. This structure provides a stunning picture of the G protein-activated receptor complex ( $R^*$ – $G$ ). What the structure alone cannot reveal is the allosteric mechanism that links interaction of a G protein with the receptor to GDP release: the  $R^*$ - and GDP-binding sites are separated by  $39\text{ \AA}$ . We first predicted<sup>8</sup> and later demonstrated by using double electron-electron resonance (DEER) experiments<sup>9</sup> that receptor-mediated GDP release is accompanied by opening of the interface between the GTPase and helical domains in the  $G\alpha_i$  subunit. Although the loss of interaction between the domains is confirmed by the crystal structure of the  $\beta_2AR$ – $G_s$  complex, the authors suggested that the exact location of the helical domain may be influenced by the process of crystallization<sup>7</sup>. To better understand receptor-mediated G-protein activation, we combined DEER data with the structure of the  $\beta_2AR$ – $G_s$  complex<sup>7</sup> to construct a unified model of the complex of activated rhodopsin with heterotrimeric  $G\alpha_i\beta\gamma$  ( $R^*$ – $G_i$ ). The model proposes that the C terminus of  $G\alpha$  triggers conformational changes leading to GDP release and concomitant domain opening. This unified model is consistent with published EPR, deuterium-exchange and EM data. The current study has resulted in the development of a structural hypothesis for the receptor– $G_i$  complex, supported by experimental data. From this structural model, we performed energetic

analysis by using the Rosetta force fields and identified residues that show marked energetic changes between the free G protein and G protein bound to activated receptor. We propose a mechanism, based on the energetic analysis, for receptor-mediated GDP release from the G protein. Finally, we validated this hypothesis with DEER, continuous wave (CW)-EPR, fluorescence and mutagenesis and found that it was consistent with previous EM and hydrogen/deuterium (H/D)-exchange experimental data.

## RESULTS

Our strategy included construction of a comparative model for the interaction of activated rhodopsin with  $G_i$  that unifies available experimental data with crystallographic data (Fig. 1 and Supplementary Movie 1). We constructed the receptor-unbound model of  $G\alpha_i\beta\gamma$  with Rosetta, on the basis of PDB 1GOT<sup>10</sup>. The model provides a higher resolution than does the structure of any other  $G_i$  family member<sup>9,10</sup> (alignment in Supplementary Fig. 1). The receptor-bound model of  $R^*$ – $G\alpha_i\beta\gamma$  is based on the crystal structure of the  $\beta_2AR$ – $G_s$  complex (PDB 3SN6 (ref. 7); alignment in Supplementary Fig. 2). Energetic minimization of the structure used Rosetta's relaxation protocol with full-atom energy potentials, including membrane-specific terms to accommodate the receptor<sup>11,12</sup>. Rosetta's refinement and force fields are capable of identifying native structures and recovering protein backbone and side chain conformations at atomic-detail accuracy<sup>13</sup>. The purpose was to allow the sequence-dependent interactions to transition from the template structure to the interactions defined by the sequence of the target (Supplementary Fig. 3d). The model with the lowest Rosetta energy was the starting point for several simulations that maximize consistency with all experimental data. We systematically compared free heterotrimeric  $G\alpha_i\beta\gamma$  to the receptor-bound form and

<sup>1</sup>Department of Chemistry, Vanderbilt University, Nashville, Tennessee, USA. <sup>2</sup>Department of Pharmacology, Vanderbilt University, Nashville, Tennessee, USA. <sup>3</sup>Department of Molecular Physiology and Biophysics, Vanderbilt University, Nashville, Tennessee, USA. <sup>4</sup>These authors contributed equally to this work. Correspondence should be addressed to H.E.H. (heidi.hamm@vanderbilt.edu) or J.M. (jens.meiler@vanderbilt.edu).

Received 18 January; accepted 2 October; published online 1 December 2013; doi:10.1038/nsmb.2705

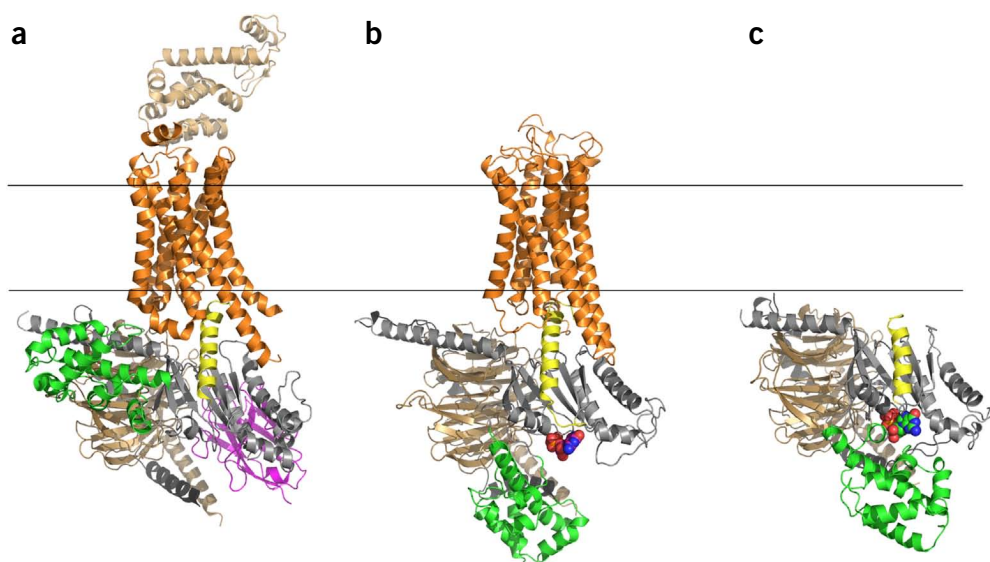


**Figure 1** Overall structure of  $\beta_2$ AR–G<sub>s</sub> complex, our model of the R\*–G<sub>i</sub> complex and the unbound G<sub>i</sub> heterotrimer. (a) Crystal structure of  $\beta_2$ AR–G<sub>s</sub> complex (PDB 3SN6 (ref. 11)). The  $\alpha 5$  helix of G<sub>s</sub> is displaced 6 Å toward the receptor, and the helical domain (green) is displaced toward the membrane interface. (b) Unified model of the R\*–G<sub>i</sub> complex. According to DEER measurements, the displacement of the helical domain (green) is on average a 15-Å translation and 62° rotation after receptor binding. (c) G<sub>i</sub> heterotrimer constructed as a comparative model from the G<sub>i</sub> (PDB 1GOT<sup>10</sup>) structure. Orange, receptor; gray, G $\alpha$  GTPase domain; green, G $\alpha$  helical domain; light brown, G $\beta$ ; black, G $\gamma$ ; magenta, nanobody; sand, T4 lysozyme; spheres, GDP.

analyzed amino acid interactions across key interfaces between and within the two proteins. Thereby we identified residues that contribute to the stabilization of both states. We additionally mapped how these key interactions are altered when G $\alpha_i$  interacts with R\*.

#### G $\alpha$ C-terminal helix interactions trigger domain opening

We observed a 5.7-Å translation and 63° rotation of the  $\alpha 5$  helix. Our energetic analysis of this conformational change linked receptor-mediated changes in the  $\alpha 5$  helix to the  $\beta 6$ – $\alpha 5$  loop, the  $\alpha 1$  and  $\alpha G$  helices and the GDP-binding site. We hypothesize that disruption of contacts between these entities and the helical domain leads to domain separation. We determined an ensemble of models of the open state that match published data, and the ensemble reflects a wider space sampled by the helical domain than that presented in our recent work<sup>9</sup>, which was published before the crystallographic structure of the complex<sup>7</sup> was published. This unified model is overall consistent with the structure of the complex, with differences in the magnitude of domain separation.

#### Exploring possible locations of the helical domain

Although qualitatively consistent with the  $\beta_2$ AR–G<sub>s</sub> complex, the placement of the helical domain in the unified model is less dramatic than that seen in the crystal structure<sup>7</sup>, on the basis of our DEER experiments for the R\*–G<sub>i</sub> complex<sup>9</sup> (Supplementary Tables 1 and 2). Average distances between residues in the helical and GTPase domains are less than the distances observed in the crystal structure of the  $\beta_2$ AR–G<sub>s</sub> complex. Although the average interdomain distance is less than that seen in the crystal structure, the distribution of these distances is wide, results consistent with a highly flexible helical domain that explores a range of conformations in the nucleotide-free state, as observed with electron crystallography<sup>13</sup>. Crystallization may stabilize a conformation that is not well populated in solution studies, whereas DEER captures an ensemble of conformations. We explored the possible positions of the helical domain of G $\alpha_i$  upon receptor

binding through rigid-body docking with subsequent reconstruction of loop regions and energy minimization. This protocol resulted in a pool of 739 models of the receptor-bound state with different positions of the helical domain.

#### Helical-domain positions consistent with EPR distances

From this pool of docked complexes, we selected an ensemble of nine models that collectively best reproduced the distance probability distributions of five different DEER distance measurements<sup>9</sup> between pairs of spin-labeled residues (Fig. 2b). In comparison, the ensemble of models for the basal state generated from Rosetta relaxation is less variable (Fig. 2a). We converted distances between C $\beta$  atoms (C $\beta$ –C $\beta$  distances) measured in the models to DEER distance probability distributions<sup>14,15</sup>. For a given ensemble of models, we compared these probability distributions with the DEER measurements (Supplementary Table 2)<sup>16</sup>. We compared the experimentally observed distance distributions with the distance distributions of the final ensemble model of the R\*–G<sub>i</sub> complex (Fig. 3a).

Superimposition of G $\alpha$  of the generated conformations with the crystal structure of  $\beta_2$ AR<sup>7</sup> indicated that there are structures that agree to within an r.m.s. deviation of 2.2 Å. This demonstrated that the location of the helical domain seen in the crystal structure was sampled because there are G $\alpha$  conformations similar to that of the G $\alpha$  of the  $\beta_2$ AR structure. This is important because these conformations could have been selected for the model ensemble if needed for agreement with the EPR data. That these conformations were not selected, i.e., were not needed for good agreement with the EPR data, suggests that they were not appreciably contributing to the conformational space sampled in our experiments.

#### The ensemble is consistent with single-particle EM data

Westfield and co-workers<sup>13</sup> performed single-particle EM analysis to examine the architecture of agonist-occupied  $\beta_2$ AR in complex with the

**Figure 2** Placement of helical domain and rotation of  $\alpha 5$  as observed by EPR measurements. (a,b)  $G_i$  in the basal state (a) and bound to activated receptor  $R^*$  (b). To illustrate motion, landmark residues are colored: red, L092; green, E122; yellow, D158; cyan, V335; blue, I343. In both cases, an ensemble of models that collectively fit the experimental data best is shown. Bottom, space-filled representations of the helical domain, illustrating its positions for the respective states.

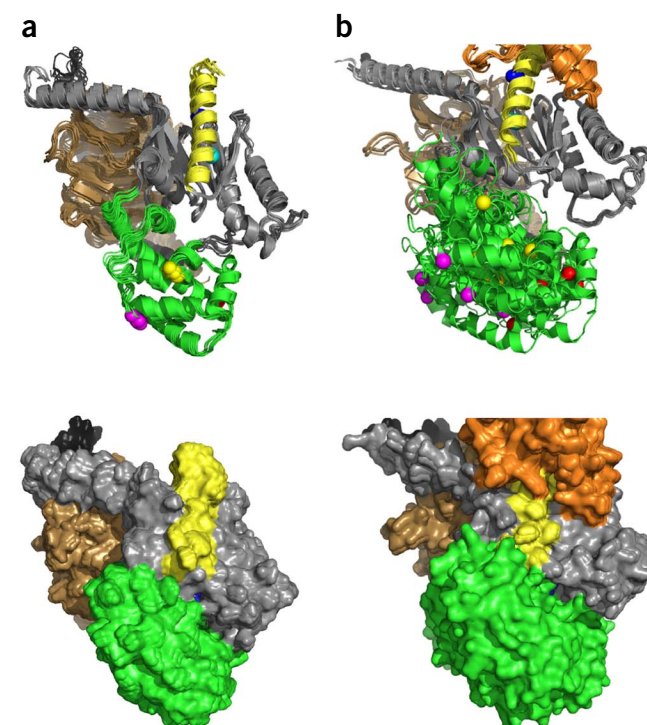
heterotrimeric G protein  $G\alpha_s\beta\gamma$ . In their experiments, the nanobody (N $\beta$ 37)-bound helical domain is variable in location, occupying a conformational space similar to that sampled by the helical domain in our ensemble (Fig. 3d and Supplementary Movie 2). The space sampled by the helical domain overlaps to a large part with the region occupied by the helical domain and nanobody in the EM study<sup>13</sup>. The slight deviations observed can perhaps be attributed to the negative-stain-EM sample preparation, which may restrict the motion of the helical domain. Regardless, there is overall agreement between the EM structure and our unified model built on DEER restraints.

### Agreement of model with accessibility data

To compare the unified model with accessibility information derived from CW-EPR and H/D-exchange experiments, we computed the relative solvent-accessible surface area for unbound and receptor-bound states of  $G_i$ . We compared the amplitude and direction of this change in exposure to the experimental values, which had been classified into five bins (large increase, small increase, neutral, small decrease and large decrease; Supplementary Tables 3 and 4). As expected, we generally found that the predicted changes in accessibility exhibit similar trends to those seen in the experimental data (Fig. 3b,c). The correlation coefficients are 0.33 for the CW-EPR measurements and 0.56 for the H/D-exchange data. No perfect correlation is expected because (i) experiments capture additional aspects beyond amino acid exposure, and (ii) exposure is estimated from the C $\beta$  position alone. Small deviations from perfect agreement were expected because the experimental data depend not only on solvent accessibility but also on side chain and backbone dynamics only incompletely considered in this model.

### Energetic analysis of inter- and intradomain interfaces

We examined the stabilizing interactions between key interfaces in  $G\alpha_i$  by using Rosetta before and after receptor binding. Specifically,



we studied four interfaces:  $G\alpha_i$  helical domain- $G\alpha_i$  GTPase domain; GDP- $G\alpha_i$  GTPase domain; C-terminal helix  $\alpha 5$ - $G\alpha_i$  GTPase domain; and  $R^*$ - $G\alpha_i$  GTPase domain. We determined interactions that stabilize these regions before and after receptor activation<sup>17</sup>.

### $G\alpha_i$ helical-domain- $G\alpha_i$ GTPase and GDP- $G\alpha_i$ GTPase interfaces

The helical domain is held in place by interactions of  $\alpha 1$  (E043, T048, K051, K054 and I055) with  $\alpha A$  (E65) and  $\alpha F$  (Q171, L175; 5.5 Rosetta energy units (REUs), which correlate with kcal per mol<sup>18</sup>; Fig. 4a, Supplementary Table 5 and Supplementary Movie 3). The helical domain is also fixed by electrostatic interactions of  $\alpha G$  (K270 and K277) and  $\beta 4$ - $\alpha 3$  (V233 and E238) loops with  $\alpha A$  (R090) and the  $\alpha D$ - $\alpha E$  loop (R144, Q147 and D150) and the  $\alpha F$ - $\beta 2$  loop (R178; 4.3 REU). Lastly, the interface is stabilized by a contact between GDP and

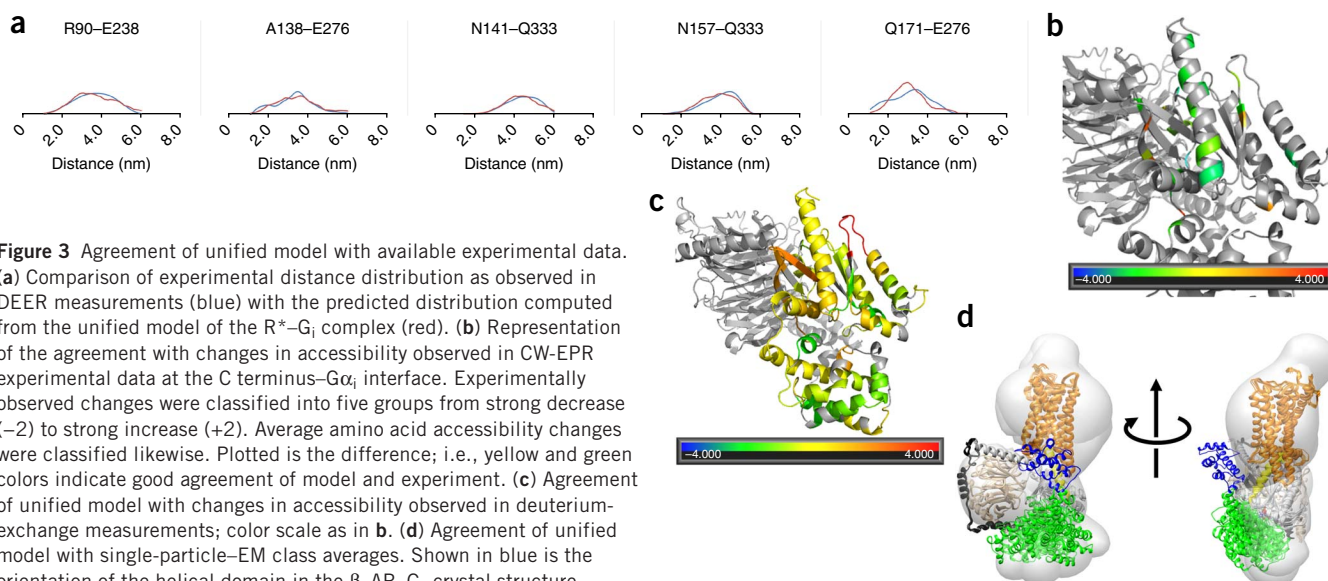


**Figure 3** Agreement of unified model with available experimental data. (a) Comparison of experimental distance distribution as observed in DEER measurements (blue) with the predicted distribution computed from the unified model of the  $R^*$ - $G_i$  complex (red). (b) Representation of the agreement with changes in accessibility observed in CW-EPR experimental data at the C terminus- $G\alpha_i$  interface. Experimentally observed changes were classified into five groups from strong decrease (-2) to strong increase (+2). Average amino acid accessibility changes were classified likewise. Plotted is the difference; i.e., yellow and green colors indicate good agreement of model and experiment. (c) Agreement of unified model with changes in accessibility observed in deuterium-exchange measurements; color scale as in b. (d) Agreement of unified model with single-particle-EM class averages. Shown in blue is the orientation of the helical domain in the  $\beta_2AR$ - $G_s$  crystal structure.

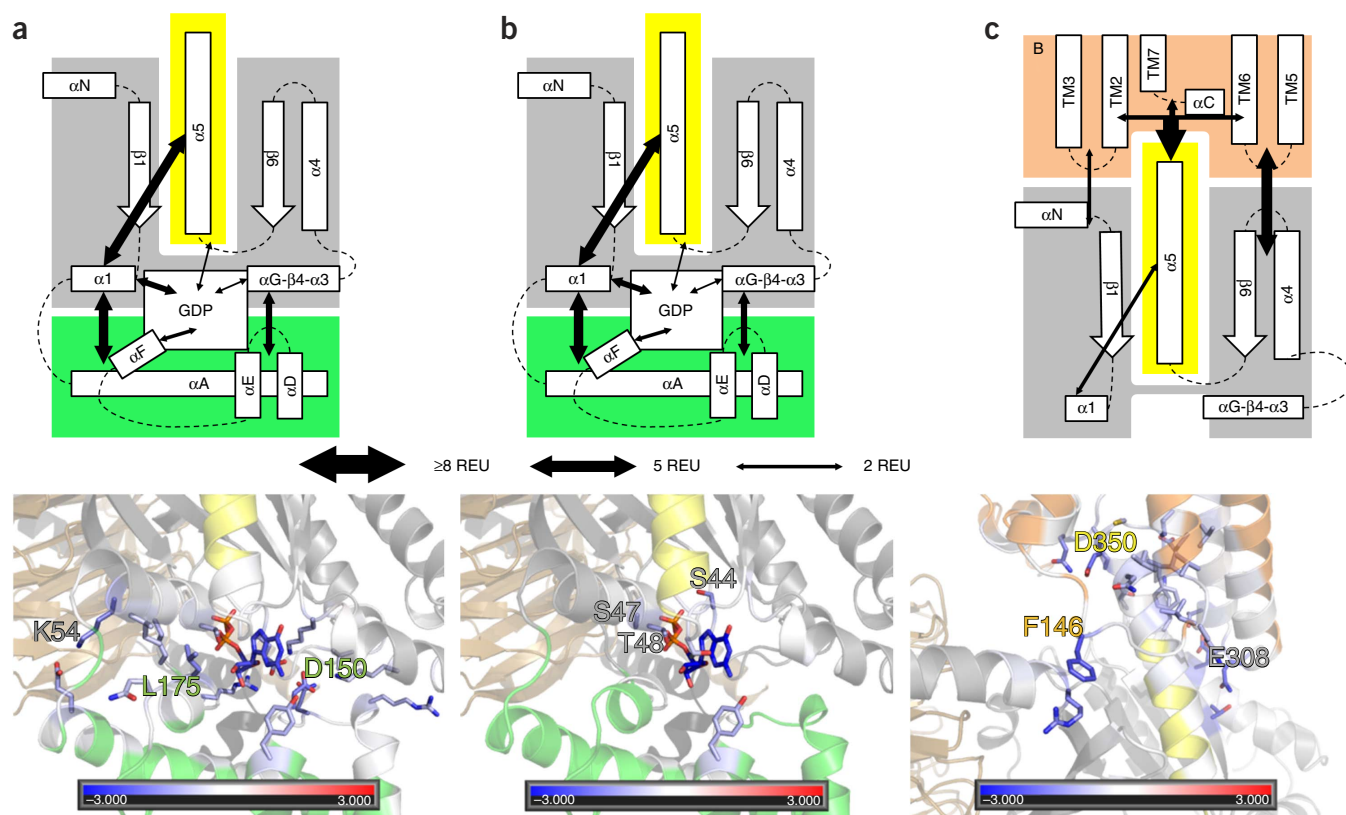


**Figure 4** Rosetta energetic analysis. (a) Analysis of energetics of helical domain– $G\alpha_i$  interface in free  $G\alpha_i$ . The thickness of arrows at top corresponds to the strength of the interaction in Rosetta energy units (REU). Residues at bottom are colored by the interaction energy REU from red (repulsive) over white (neutral) to blue (attractive). Residues that contribute  $>0.5$  REU are displayed as sticks, and the three residues with the largest contributions are labeled. (b) Energetics of the GDP– $G\alpha_i$  interface in free  $G\alpha_i$ . (c) Energetics of  $R^*$ – $G\alpha_i$  interface in the  $R^*$ – $G\alpha_i$  complex.

the  $\alpha D$ – $\alpha E$  loop (Y154; 2.0 REU). The total interaction energy is approximately 10.1 REU. GDP is stabilized through interactions with  $\alpha 1$  (S044, S047 and T048; 3.1 REU), the helical domain (Y154, 0.8 REU) and the  $\beta 6$ – $\alpha 5$  loop (T327; 0.9 REU). The total interaction energy is approximately 5.1 REU (Fig. 4b, Supplementary Table 5 and Supplementary Movie 4).

#### Receptor-bound $R^*$ – $G\alpha_i$ GTPase-domain interface

The  $G\alpha$  C-terminal peptide (I344, N347, L348, D350, C351, L353 and F354) binds to the receptor through transmembrane domains (TMs) TM3 (V138, V139 and K141), TM6 (E249 and V250) and TM7– $\alpha C$  loop (K311 and Q312; 8.2 REU; Fig. 4c, Supplementary Table 5 and Supplementary Movie 5). Further, intracellular loop 2 (F146) interacts with the  $\alpha N$ – $\beta 1$  loop at R32 (2.2 REU). The extended intracellular loop 3 (Q237, S240, T242 and T243) interacts with  $\alpha 4$  (E308), the  $\alpha 4$ – $\beta 6$ –loop (D315 and K317) and  $\beta 6$  (T321; 5.6 REU). The total interaction energy was approximately 17.2 REU. Comparison of residue distances for this interface with the coordinates of the  $\beta_2AR$ – $G_s$  complex structure indicated that residue E249 changes interactions most drastically, whereas the model ensemble showed small variation in the interface distances (Supplementary Table 6).

#### Rewiring of $\alpha 5$ – $G\alpha_i$ GTPase interface upon receptor interaction

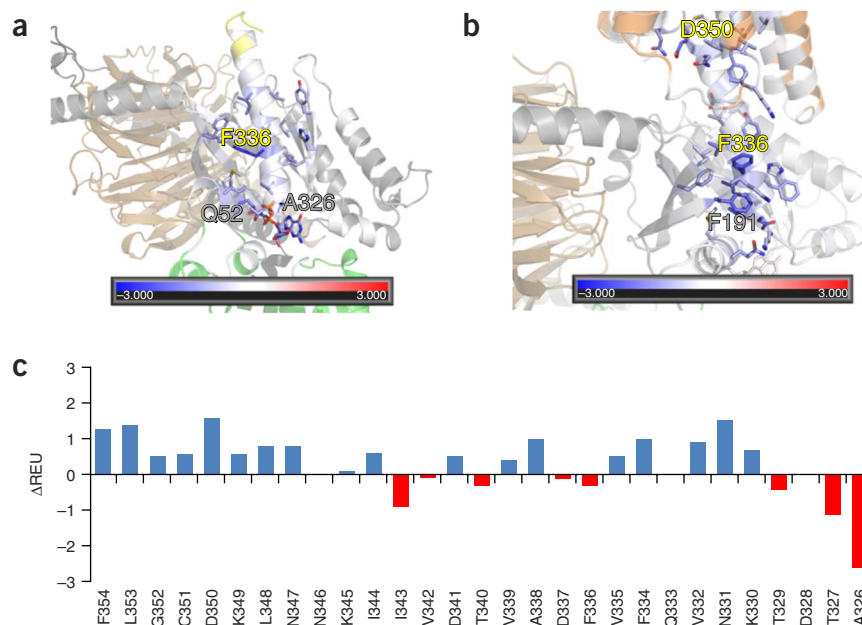
In the basal state, the C-terminal helix  $\alpha 5$  of  $G\alpha_i$  (N331, V332, Q333, V335, F336, A338, V339, T340, V342 and I343) interacts favorably with  $\beta 2$ ,  $\beta 3$ ,  $\beta 5$  and  $\beta 6$  (F191, F196, I265, F267, Y320 and H322; 6.4 REU) and  $\alpha 1$  (T048, Q52, M053 and I056; 5.0 REU; Fig. 5a,

Supplementary Table 5 and Supplementary Movie 6). The  $\beta 6$ – $\alpha 5$  loop (A326, T327 and T329) interacts with  $\alpha 1$  (T048 and Q052; 2.5 REU) and GDP (1.4 REU).

Upon interaction with the activated receptor (Fig. 5b and Supplementary Movie 7), the  $\alpha 5$  helix (I344, N347, L348, K349, D350, C351, G352, L353 and F354) experiences an attraction to the receptor of 8.6 REU. This attractive interaction moves the  $\alpha 5$  helix 5.7 Å toward the receptor and triggers a rotation of the  $\alpha 5$  helix by 63° (Supplementary Movie 8). This is accompanied by a loss of helicity at the base of the  $\alpha 5$  helix, which is in proximity to bound nucleotide in the inactive heterotrimer. Thus, the base of the  $\alpha 5$  helix appears to ‘melt’ in the nucleotide-free state. The interaction of the  $\alpha 5$  helix with  $\beta 2$ ,  $\beta 3$ ,  $\beta 5$  and  $\beta 6$  is modified and strengthened (F191, K192, L194, F196, I265, F267, E318, Y320 and H322; 10.3 REU) upon interaction with activated receptors. At the same time, interactions of the  $\alpha 5$  helix with  $\alpha 1$  (T048, Q52, M053 and I056; 2.2 REU) and GDP (0.2 REU) are substantially weakened. This was accompanied by loss of helical structure at the top of the  $\alpha 1$  helix, thus effectively elongating the linker region between the GTPase domain and the helical domain and possibly facilitating domain separation. A summary of residue stabilizations and destabilizations is shown in Figure 5c.

Interactions of residues E249 and E311 of  $R^*$  changed most drastically from the coordinates of the  $\beta_2AR$ – $G_s$  complex structure<sup>7</sup>, as measured by the change in distance to other residues in the interface. Also, the model ensemble showed small variation in the interface distances, thus indicating that the interactions were consistently predicted (Supplementary Table 7).

**Figure 5** Rosetta energetic analysis of the interface between  $\alpha 5$  and  $G\alpha_i$  GTPase. (a) Basal-state energetics. (b) Energetics of the  $R^*-G\alpha_i$  complex. Residues are colored by the interaction-energy REU from red (repulsive) over white (neutral) to blue (attractive). Residues that contribute  $>0.5$  REU are displayed as sticks, and the three residues with the largest contributions are labeled. (c) Energy change ( $\Delta$ REU) of C-terminal residues ( $\beta 6$ - $\alpha 5$  loop and  $\alpha 5$  helix) upon receptor binding. Blue indicates stabilization and red, destabilization.



### Helical-domain position verified by DEER distances

We prepared double-cysteine mutants in positions 29( $\alpha N$ )-68( $\alpha A$ ) and 29( $\alpha N$ )-83( $\alpha A$ ) to independently verify the position of the helical domain with respect to the GTPase domain in the unified model and to differentiate it from the  $\beta_2AR-G_s$  crystal structure<sup>7</sup>. We used a cysteine-depleted  $G\alpha_i$  parent protein as a starting point for these studies, labeling cysteine mutants with a thiol-selective nitroxide probe, testing them for functionality and determining distances by DEER<sup>19-21</sup>. Before receptor activation, the major populations in the distribution of positions 29-68 and 29-83 were centered at  $\sim 31$  Å and  $\sim 49$  Å, respectively. This was consistent with the model for the unbound state (Supplementary Fig. 4a and Supplementary Table 1). Upon receptor activation, the distribution was centered at  $\sim 32$  Å and  $\sim 45$  Å, respectively. These results were in agreement with the receptor-bound ensemble in the unified model (Fig. 6a) but different from results seen in the  $\beta_2AR-G_s$  crystal structure, which predicts a substantial reduction of these distances (Supplementary Fig. 4b). These results suggest that the helical domain may have been stabilized in an extreme orientation in the crystal structure. Nevertheless, the loss of observed interdomain contacts in the crystal structure is in overall agreement with our model. Our model supports a range of motion

for the helical domain upon receptor activation, and the crystal structure may represent an extreme value along the continuum of possible orientations for the helical domain during signaling.

### Verification of the $\alpha 5$ -helix rotation and translation

We prepared one double mutant in positions 29( $\alpha N$ )-330( $\alpha 5$ ) in order to test the intramolecular rearrangement of  $\alpha 5$  after receptor activation. Both unified model and crystal structure<sup>7</sup> predict a contraction of this distance. The observed distance distributions were consistent with this prediction, although the reduction was not as pronounced as in the model (comparison of Fig. 6a and Supplementary Fig. 4a). The ensemble of models gives a reduction of 5.0 Å, which is in agreement with the 2.2-Å experimental distance change. Specifically, the DEER distance distributions showed a change from 30.7 Å to 28.5 Å, as calculated from their weighted averages. The ensemble of models shows a change from 31.3 Å to 26.3 Å in going from the receptor-unbound to receptor-bound states.

We measured the number of nearest neighbors in our model to predict changes in solvent accessibility in the  $\beta 2$  strand and the

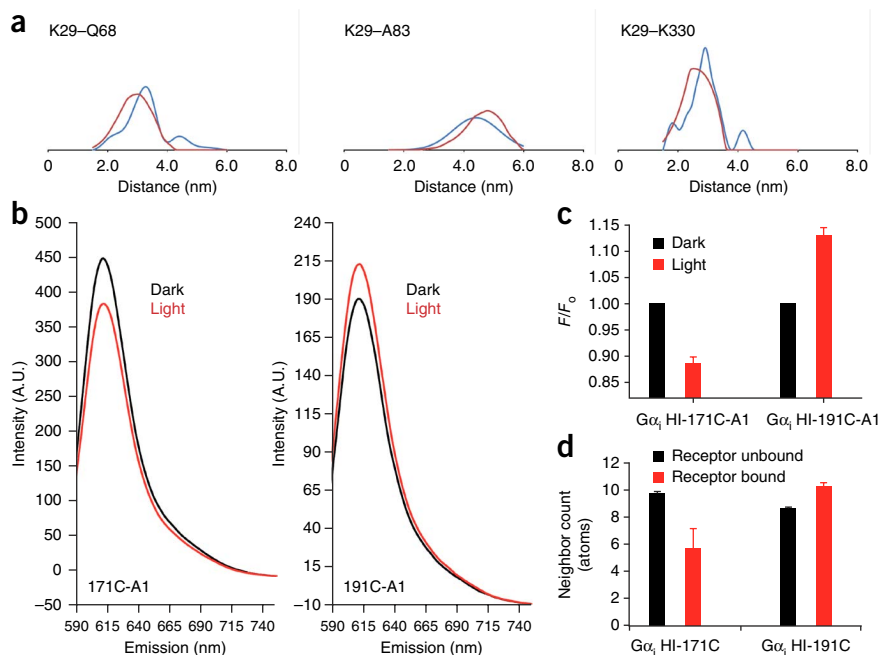


**Figure 6** Agreement of unified model with new structural data. (a) Comparison of the experimental distance distribution as observed in DEER measurements (blue) with the predicted distribution computed from the ensemble mode of the  $R^*-G_i$  complex (red). (b-d) Comparison of accessibility of residues 171 and 191 in  $G\alpha_i$  in the basal (black) and activated (red) states. (b) Residues 171 and 191 in a  $G\alpha_i$  protein were specifically modified with Alexa Fluor (A1), and emission was scanned at A1-specific wavelengths. (c) Measured fluorescence of cysteine mutants labeled with a fluorescent probe. Data represent the mean + s.e.m. from three independent experiments. (d) Predicted burial as indicated by neighbor count on the basis of the unified model. Data represent mean calculated over the ensemble of models +s.d.

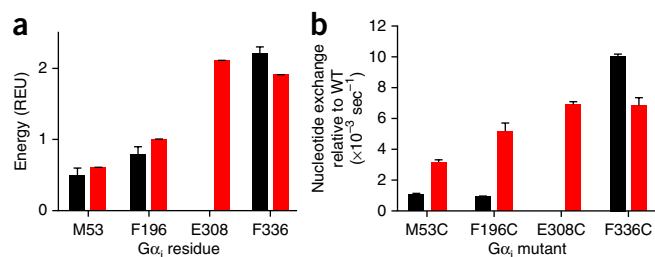


**Figure 7** Validation of the model energetic predictions. **(a)** The predicted energetic contribution to a given residue's corresponding interface is plotted for basal (black) and stimulated (red) states. Residues M53, F196 and F336 are within the  $\alpha 5$ - $G\alpha_i$  interface. Residue E308 is within the  $R^*$ - $G\alpha_i$  interface, and therefore no interface contributions are predicted in the basal state. Energy is given in REU. Data represent mean + s.d. **(b)** Basal and receptor-mediated nucleotide-exchange rates.  $G\alpha_i$ -mutant exchange rates are shown as the absolute value of the difference of the nucleotide-exchange rate relative to wild-type  $G\alpha_i$  in both basal and receptor-mediated states. Data represent six independent experiments; error bars, s.e.m. WT, wild type.

linker between the  $\alpha$ -helical and GTPase domain. With this method, the solvent accessibility of F191, located in the  $\beta_2$  strand, is predicted to decrease upon activation, whereas solvent accessibility of Q171, located in one of the linkers between the  $\alpha$ -helical and GTPase domain, is predicted to increase (Fig. 6d). As an independent verification of our model, we individually mutated each of these residues to cysteine in a  $G\alpha_i$  protein lacking solvent-exposed cysteines. We then labeled each mutant protein with a fluorescent probe and examined the polarity of the environment of the labeled residues before and after receptor activation. Increases in solvent exposure increase the polarity reported by the probe, as reflected by a reduction in the fluorescence emission. An increase in the hydrophobicity of the probe's environment is typically reflected by an increase in emission from the labeled residue. As predicted by our model, residue 171 exhibited a decreased fluorescence upon receptor activation as compared to that of the inactive state (Fig. 6b,c), thus suggesting a more solvent-exposed environment for this residue upon domain separation. This is consistent with its location in the linker region between the helical and GTPase domains. However, F191 is located in the GTPase domain, packed between the  $\beta_2$  sheet and  $\alpha 5$ . We observed an increased emission from labeled residue 191 upon receptor activation (Fig. 6b,c) consistent with the increase in nearest neighbors predicted by our model. The increase and decrease in solvent exposure that we observed for residues 171 and 191, respectively, were also consistent with mobility data previously reported for these residues (Supplementary Tables 3 and 4). This is also consistent with a recent study identifying a more solvent-excluded environment for the  $\beta_2$ - $\beta_3$  loop upon receptor activation<sup>22,23</sup>. Thus, these new data provided independent validation of the predictions from the current model, in regions predicted to show both increases and decreases in solvent accessibility upon receptor activation.

We used four critical interface regions to test our model experimentally, in both basal and receptor-activated states. M53 is in the interface of the  $\alpha 1$  helix and the  $\alpha 5$  helix and was predicted to stabilize this interaction. F196 is in the  $\beta 3$  sheet and was also predicted to stabilize the interaction with the  $\alpha 5$  helix. E308 is in the  $\alpha 4$  helix and is critical for interaction with the receptor. All four residues were predicted by the model to be critical to stabilize the stimulated state; all but E308 were predicted to be critical residues stabilizing the basal state. We mutated each residue to a cysteine, tested basal and receptor-mediated GTP and GDP exchange for each of the mutants relative to wild type (Fig. 7b) and compared them to the predicted Rosetta

interface energies (Fig. 7a). The basal exchange of E308C was determined experimentally but was not significantly different from wild type, as was predicted by the model. Calculations used the ensemble of models, which contain the native sequence for heterotrimer and receptor. The predicted and experimental values were consistent with each other (Supplementary Table 8), thus further supporting the predictive ability of our model for identifying residues critical for receptor interaction and nucleotide exchange.

## DISCUSSION

In the current study, we highlighted changes in the orientation of the C-terminal  $\alpha 5$  helix relative to its orientation in inactive heterotrimer before binding to receptor. The energy associated with the interface of the  $\alpha 5$  helix and surrounding regions is critically important for GDP binding and receptor-mediated GDP release. We used the  $\beta_2$ AR- $G_s$  complex as a template for creating a homology model of the rhodopsin- $G_i$  heterotrimer complex that is the focus of our current model. We compared important interactions of  $G\alpha$  within the rhodopsin- $G_i$  complex to the interactions that the same regions exhibit in the inactive heterotrimer, in the absence of activated receptor. We then compared the orientation of the helical domain in the rhodopsin- $G_i$  complex to that of the helical domain in the  $\beta_2$ AR- $G_s$  crystal structure<sup>7</sup> in order to better understand the similarities and differences between the orientations afforded by the two different systems and methodologies involved.

There are some potential drawbacks inherent in our approach, such as perturbations of the system by the introduction of spin labels or fluorescent probes. These can potentially perturb the biologically relevant conformation on a local or global level. Each experimental approach is aimed at a particular system under unique conditions. Coverage of experimental data is nonuniform, thus resulting in regions of high confidence supported by multiple data sets and regions of low confidence where data are sparse and/or affiliated with large error. Because of this, observations from different approaches and systems are not likely to be identical, nor do we expect them to be. Therefore, the hybrid model presented herein, like all models, is not likely to be correct in every detail but is consistent with the current state of existing knowledge. The power of such a model is that it presents an atomic-detail hypothesis of the structure and energetics, thereby creating a roadmap for future experimental studies that can verify or reject parts of the model. In an iterative fashion, a completely verified atomic-detail model of the system can then be constructed.

The present analysis is specific for the rhodopsin- $G\alpha_i\beta\gamma$  complex.  $G_i$  is a close  $G_t$  family member that also couples to rhodopsin<sup>24</sup>. We used  $G_i$  for all experiments and modeling instead of  $G_t$  because  $G_t$  does not express well. As a result, the experimental EPR data used as restraints during modeling were specific for the rhodopsin- $G\alpha_i\beta\gamma$  complex. The energetic analysis, which is sequence dependent, was also specific for the rhodopsin- $G\alpha_i\beta\gamma$  complex. Mutational studies conducted on this specific system confirm our model.

To what extent the findings can be generalized to other G protein-coupled receptor (GPCR)-G protein systems is an important question that remains to be determined. The location of the helical domain as described by the structural ensemble is likely to be sampled in other GPCR-G protein systems. The mechanistic model resulting from use of the crystal structure ( $\beta_2$ AR- $G_s$ )<sup>7</sup> as a template, as was used here, would be expected to be similar to the extent that all GPCR-G protein systems exhibit some degree of similarity. However, specific, sequence-dependent differences are likely to contribute to the differences we observe, at both the G-protein and GPCR levels. A more rigorous and experimentally dense study focused on the individual

proteins of interest will be required to study the same interactions in the  $\beta_2\text{AR-G}_s$  or other GPCR-G protein systems.

The mechanism of receptor-mediated G-protein activation has been previously investigated. A 'sequential release mechanism' proposes that binding of the C terminus of  $G\alpha$  allosterically causes the release of GDP<sup>25,26</sup>. This qualitative observation agrees with our model, which quantitatively describes the importance of the various interactions leading to GDP release. Another previous study used molecular modeling to investigate the mechanism of GDP release from  $G\alpha$  upon receptor binding<sup>25</sup>. Consistently with our results, the authors propose that a rotation of  $\alpha 5$  is a critical step toward GDP release and implicate the  $\beta 6$ - $\alpha 5$  loop as having a key role in propagating the signal to GDP<sup>25</sup>; this has been supported in a mutational study examining rates of nucleotide release<sup>27</sup>. This study implicated an interaction between the intracellular loop 2 (IL2) of the receptor and the N terminus of  $G\alpha$ , an interaction that our energetic analysis independently identifies as an important interaction between R\* IL2 with the  $\alpha\text{N}$ - $\beta 1$  loop<sup>28</sup>. Molecular-dynamics investigations of GDP release from  $G\alpha_i\beta\gamma$  conducted in the absence of receptors have suggested that several residues may be important in interactions with GDP, including S44, S47 and T327 (ref. 29). Molecular dynamics was also used to examine the structural changes that the  $G\alpha$  subunit of transducin ( $G\alpha_t$ ) undergoes to release GDP<sup>30</sup>, again in the absence of receptors. Thus, the inclusion of activated receptor in the current study presents a major advance in efforts to model the changes in  $G\alpha$  that occur upon receptor activation.

We determined the relative conformational space sampled by the helical domain within the ensemble to the GTPase domain of  $G\alpha$  by using DEER. Given the small number and large uncertainty of the EPR distance measurements, the nine conformations represented in the stimulated, receptor-bound state formed a representative ensemble of conformations sampled. Furthermore, the relative conformational space sampled by the helical domain within the ensemble was wider than that in our previous model, which does not take into account the distribution of distances between labeled residues upon receptor activation. This relatively wide distribution resulted in an ensemble of models that may represent the dynamic changes in the orientation of the helical domain that accompany receptor-mediated GDP release in a physiologically relevant environment.

Other regions of the model that were derived primarily from the crystallographic template are necessarily less flexible. Because our modeling template was based on the crystal structure<sup>7</sup>, the model accuracy in these regions was sufficiently high to approach atomic detail. Therefore, we report precise values for the 5.7-Å shift and 63° rotation of the  $G\alpha$  C terminus with respect to its orientation in the inactive heterotrimer. In these regions, our analysis of the energetic contributions to the stability of specific interfaces between regions of  $G\alpha$  in the inactive heterotrimer and receptor-bound activated complex led to the current model of the mechanism of receptor-mediated nucleotide release.

The recent determination of the crystal structure of the  $\beta_2\text{AR-G}_s$  protein complex<sup>7</sup> provides the atomic-detail insight into the interaction of a G protein with an active GPCR that we required in order to complete the present study. The availability of this experimental structure is a milestone that greatly advanced understanding of the structural determinants of the receptor-G protein complex. Using primary data and computational modeling, and taking into account the crystal structure of the  $\beta_2\text{AR-G}_s$  complex, we obtained an ensemble of structurally dynamic states consistent with mutational, biophysical and structural studies that are currently available. In our model, the average interdomain separation is less dramatic than that seen

in the crystal structure, possibly owing to the crystallization process (Supplementary Table 9), but it is in qualitative agreement with it as well as with cryo-EM studies. This model integrates data from multiple published studies and provides a detailed energetic pathway for signal transduction between activated receptor and  $G_i$  protein. It thereby creates a pathway to elucidate the structural and energetic determinants of signal transduction between activated receptor and  $G_i$ .

In summary, on the basis of DEER distance measurements and the hybrid model, the rhodopsin- $G_i$  complex is best represented as a structural ensemble allowing GDP release and opening of the interdomain cleft and the  $G\alpha$  helical domain to sample multiple orientations. The hybrid model here represents elements from both the  $\beta_2\text{AR-G}_s$  crystal structure<sup>7</sup> and dynamic conformational changes that occur in solution as the G protein interacts with activated receptor to catalyze the release of GDP. Thus, this work provides a framework and a roadmap for future experiments including high-resolution modeling of the receptor-G protein complex.

## METHODS

Methods and any associated references are available in the [online version of the paper](#).

Note: Any Supplementary Information and Source Data files are available in the [online version of the paper](#).

## ACKNOWLEDGMENTS

Work in J.M.'s laboratory is supported through the US National Institutes of Health (NIH) (R01 GM080403, R01 MH090192 and R01 GM099842) and US National Science Foundation (Career 0742762). NIH National Research Service Award (MH086222) provided additional support (N.S.A.). Work in the laboratory of H.E.H. is supported through the NIH (EY006062 to H.E.H.). NIH provided additional support (U54 GM084757 to R.A.S.). The authors would like to thank S. Deluca of Vanderbilt University for implementing the Rosetta per-residue interface energy tool and H. Mchaourab of Vanderbilt University for his support with the DEER measurements (support to NIH S10 RR027091).

## AUTHOR CONTRIBUTIONS

N.S.A., A.M.P., A.I.K., H.E.H. and J.M. designed the experiments. N.S.A., A.M.P., A.I.K. and R.A.S. collected data. All authors contributed analysis. N.S.A., A.M.P., H.E.H. and J.M. wrote the manuscript with input from A.I.K. and R.A.S.

## COMPETING FINANCIAL INTERESTS

The authors declare no competing financial interests.

Reprints and permissions information is available online at <http://www.nature.com/reprints/index.html>.

- Onrust, R. *et al.* Receptor and  $\beta\gamma$  binding sites in the  $\alpha$  subunit of the retinal G protein transducin. *Science* **275**, 381–384 (1997).
- Cai, K., Itoh, Y. & Khorana, H.G. Mapping of contact sites in complex formation between transducin and light-activated rhodopsin by covalent crosslinking: use of a photoactivatable reagent. *Proc. Natl. Acad. Sci. USA* **98**, 4877–4882 (2001).
- Mazzoni, M.R. & Hamm, H.E. Interaction of transducin with light-activated rhodopsin protects it from proteolytic digestion by trypsin. *J. Biol. Chem.* **271**, 30034–30040 (1996).
- Slessareva, J.E. *et al.* Closely related G-protein-coupled receptors use multiple and distinct domains on G-protein  $\alpha$ -subunits for selective coupling. *J. Biol. Chem.* **278**, 50530–50536 (2003).
- Marin, E.P., Krishna, A.G. & Sakmar, T.P. Disruption of the  $\alpha 5$  helix of transducin impairs rhodopsin-catalyzed nucleotide exchange. *Biochemistry* **41**, 6988–6994 (2002).
- Oldham, W.M., Van Eps, N., Preininger, A.M., Hubbell, W.L. & Hamm, H.E. Mechanism of the receptor-catalyzed activation of heterotrimeric G proteins. *Nat. Struct. Mol. Biol.* **13**, 772–777 (2006).
- Rasmussen, S.G. *et al.* Crystal structure of the  $\beta 2$  adrenergic receptor-Gs protein complex. *Nature* **477**, 549–555 (2011).
- Noel, J.P., Hamm, H.E. & Sigler, P.B. The 2.2 Å crystal structure of transducin- $\alpha$  complexed with GTP $\gamma$ S. *Nature* **366**, 654–663 (1993).
- Van Eps, N. *et al.* Interaction of a G protein with an activated receptor opens the interdomain interface in the alpha subunit. *Proc. Natl. Acad. Sci. USA* **108**, 9420–9424 (2011).
- Lambricht, D.G. *et al.* The 2.0 Å crystal structure of a heterotrimeric G protein. *Nature* **379**, 311–319 (1996).

11. Barth, P., Wallner, B. & Baker, D. Prediction of membrane protein structures with complex topologies using limited constraints. *Proc. Natl. Acad. Sci. USA* **106**, 1409–1414 (2009).
12. Barth, P., Schonbrun, J. & Baker, D. Toward high-resolution prediction and design of transmembrane helical protein structures. *Proc. Natl. Acad. Sci. USA* **104**, 15682–15687 (2007).
13. Westfield, G.H. *et al.* Structural flexibility of the G $\alpha$ s  $\alpha$ -helical domain in the  $\beta_2$ -adrenoceptor Gs complex. *Proc. Natl. Acad. Sci. USA* **108**, 16086–16091 (2011).
14. Hirst, S.J., Alexander, N., Mchaourab, H.S. & Meiler, J. RosettaEPR: an integrated tool for protein structure determination from sparse EPR data. *J. Struct. Biol.* **173**, 506–514 (2011).
15. Alexander, N., Al-Mestarihi, A., Bortolus, M., Mchaourab, H. & Meiler, J. *De novo* high-resolution protein structure determination from sparse spin-labeling epr data. *Structure* **16**, 181–195 (2008).
16. Kamarainen, J.-K. *et al.* Improving similarity measures of histograms using smoothing projections. *Pattern Recognit. Lett.* **24**, 2009–2019 (2003).
17. Kortemme, T., Kim, D.E. & Baker, D. Computational alanine scanning of protein-protein interfaces. *Sci. STKE* **2004**, pl2 (2004).
18. Kellogg, E.H., Leaver-Fay, A. & Baker, D. Role of conformational sampling in computing mutation-induced changes in protein structure and stability. *Proteins* **79**, 830–838 (2011).
19. Jeschke, G., Bender, A., Paulsen, H., Zimmermann, H. & Godt, A. Sensitivity enhancement in pulse EPR distance measurements. *J. Magn. Reson.* **169**, 1–12 (2004).
20. Borbat, P.P., Mchaourab, H.S. & Freed, J.H. Protein structure determination using long-distance constraints from double-quantum coherence ESR: study of T4 lysozyme. *J. Am. Chem. Soc.* **124**, 5304–5314 (2002).
21. Jeschke, G. & Polyhach, Y. Distance measurements on spin-labelled biomacromolecules by pulsed electron paramagnetic resonance. *Phys. Chem. Chem. Phys.* **9**, 1895–1910 (2007).
22. Hamm, H.E., Kaya, A.I., Gilbert Iii, J.A. & Preininger, A.M. Linking receptor activation to changes in Sw I and II of G $\alpha$  proteins. *J. Struct. Biol.* **184**, 63–74 (2013).
23. Preininger, A.M., Meiler, J. & Hamm, H.E. Conformational flexibility and structural dynamics in GPCR-mediated G protein activation: a perspective. *J. Mol. Biol.* **425**, 2288–2298 (2013).
24. Medkova, M., Preininger, A.M., Yu, N.J., Hubbell, W.L. & Hamm, H.E. Conformational changes in the amino-terminal helix of the G protein  $\alpha_{i1}$  following dissociation from G $\beta\gamma$  subunit and activation. *Biochemistry* **41**, 9962–9972 (2002).
25. Scheerer, P. *et al.* Structural and kinetic modeling of an activating helix switch in the rhodopsin-transducin interface. *Proc. Natl. Acad. Sci. USA* **106**, 10660–10665 (2009).
26. Kapoor, N., Menon, S.T., Chauhan, R., Sachdev, P. & Sakmar, T.P. Structural evidence for a sequential release mechanism for activation of heterotrimeric G proteins. *J. Mol. Biol.* **393**, 882–897 (2009).
27. Chung, K.Y. *et al.* Conformational changes in the G protein Gs induced by the  $\beta_2$  adrenergic receptor. *Nature* **477**, 611–615 (2011).
28. Fanelli, F. & Dell'Orco, D. Dark and photoactivated rhodopsin share common binding modes to transducin. *FEBS Lett.* **582**, 991–996 (2008).
29. Louet, M., Perahia, D., Martinez, J. & Floquet, N. A concerted mechanism for opening the gdp binding pocket and release of the nucleotide in hetero-trimeric G-proteins. *J. Mol. Biol.* **411**, 298–312 (2011).
30. Ceruso, M.A., Periole, X. & Weinstein, H. Molecular dynamics simulations of transducin: interdomain and front to back communication in activation and nucleotide exchange. *J. Mol. Biol.* **338**, 469–481 (2004).

## ONLINE METHODS

**Receptor-unbound model of  $G\alpha_i\beta\gamma$ .** The model of  $G\alpha_i\beta\gamma$  was constructed on the basis of the PDB coordinates 1GOT<sup>9,10</sup>. Missing residues were reconstructed with kinematic loop closure<sup>31</sup>. The model of the receptor-unbound state was then subjected to 100 independent relaxation trajectories that iterate between backbone perturbation, fast side chain optimization with a rotamer library<sup>32</sup> and all-atom gradient minimization in the Rosetta full-atom force field<sup>33</sup>. The ten models with lowest Rosetta energy form the conformational ensemble, which represents  $G\alpha_i\beta\gamma$  in the receptor-unbound state (structures available in **Supplementary Data Set 1**). GDP was present throughout all steps of the protocol.

**Receptor-bound  $G\alpha_i\beta\gamma$  model consistent with experimental data.** The crystal structure of the  $\beta_2AR-G_s$  complex (PDB 3SN6 (ref. 7)) was used as the template for constructing a comparative model for the rhodopsin-bound state of  $G\alpha_i\beta\gamma$ . The sequence of metarhodopsin, bovine  $G\beta_1$  and  $G\gamma_1$ , and  $G\alpha_i$  were threaded on the 3SN6 (ref. 7) crystal structure. The receptor sequence was aligned with structure-structure alignment of 3SN6 (ref. 7) with the structure of metarhodopsin from 3PQR<sup>34</sup>. A blast sequence alignment was used to align  $G\beta_1$ . For the  $\alpha$  subunit, the published sequence alignment between  $G\alpha_s$  and  $G\alpha_i$  was used<sup>35</sup>. For each chain, Rosetta kinematic loop closure<sup>31</sup> was used to construct missing coordinates. After loop construction, the model was relaxed in Rosetta 46 times. To accommodate the receptor, the relaxation used Rosetta's full-atom membrane potential<sup>11,12</sup>. The model with lowest Rosetta energy was used as the starting point for the comparative model of the  $R^*-G_i$  complex.

No agonist was present during model construction. However, comparison of the crystal structure of activated opsin (3DQB<sup>36</sup>) with the  $\beta_2AR-G_s$  complex crystal structure shows that the presence or absence of an agonist has only a small effect on the structure of the TM domain (**Supplementary Fig. 5a**). The two receptor structures can be superimposed with an r.m.s. deviation of 2.0 Å. The agonist probably stabilizes the active conformation of the  $\beta_2AR$ , whereas our goal was to model the G protein-bound activated state of native rhodopsin.

Our best-scoring model of activated rhodopsin aligned structurally to 2.5-Å r.m.s. deviation to the  $\beta_2AR-G_s$  over the entire complex. The receptor in our model agreed with the crystal structure of activated rhodopsin (PDB 3DQB<sup>36</sup>) to an r.m.s. deviation of 2.5 Å (**Supplementary Fig. 5b**). Importantly, the crystal structure of activated rhodopsin (PDB 3DQB<sup>36</sup>) could be superimposed with the  $\beta_2AR$  to 2.0-Å r.m.s. deviation. This indicates that the TM domain in the model remains in an active conformation during comparative modeling even though the agonist has not been explicitly added.

No regions of the model were assumed to be correct a priori. The goal was to refine the model with as much experimental data as was available. However, different parts of the model were influenced by different sets of data, and the backbone conformation of the receptor-G-protein complex was only slightly refined in some regions but sampled more exhaustively in others. Portions of the model were (i) based on the crystal structure template and refinement, (ii) reconstructed through comparative modeling, and (iii) positioned through EPR restraints and refinement (**Supplementary Fig. 3a-c**).

Additionally, multiple experimental data were used to validate the model for specific residues: CW-EPR (**Supplementary Table 3** and **Fig. 3b**); DEER measurements (**Supplementary Table 1**); and H/D-exchange data (**Supplementary Table 4** and **Fig. 3c**).

**Exploring possible locations of the helical domain.** The helical domain (residues 63 to 177) was separated from the rest of the nucleotide-binding domain by removal of linking residues 58–62 and 178–185. Possible placements of the helical domain were explored in 1,000 independent docking simulations. Both linker regions were reconstructed<sup>31</sup> after docking and before each of these models was relaxed in the Rosetta full-atom energy membrane potential<sup>11,12</sup>. This protocol resulted in a pool of 739 nonclashing models of the receptor-bound state with different positions of the helical domain. Detailed computational and experimental protocols are given in the **Supplementary Note**.

**Helical-domain positions consistent with DEER distances.** A subset of models were selected that optimally reproduce the DEER distances and signal shapes. DEER data were simulated for each model with the knowledge-based potential<sup>14,15</sup>. The overall score of a given ensemble of models was the sum of the scores for the five previously published DEER distance measurements<sup>9</sup>. An ensemble

of nine structures was selected from 1,000 independent Monte Carlo simulations. This ensemble gave the best agreement between experiment and model (**Supplementary Table 2**). It constitutes the ensemble of the  $R^*-G_i$  complex (structures available in **Supplementary Data Set 2**).

The distance distributions seen were in most cases too large to be explained with intrinsic flexibility of the label<sup>37</sup>. Therefore, an implicit model of the spin label is used to describe the conformational distribution of the spin label, as detailed previously<sup>16</sup>. We used this method to distinguish label distribution from backbone conformational changes. Distance K29-K330 in **Figure 6a** is an example of a distribution that is dominated by the spin-label conformational distribution, with very little contribution by backbone changes in the ensemble. Distance K29-A83 in **Figure 6a** is an example with a distribution too wide to result from label conformational changes only.

**Inter- and intradomain interface energetic analysis.** The energy values are reported in Rosetta energy units (REU), which correlate with kcal per mol<sup>18</sup>. Energies are broken down on a per-residue basis to identify positions with changing interactions upon complex formation (**Figs. 4** and **5**).

**Materials for experimental studies.** GDP and GTP $\gamma$ S were purchased from Sigma-Aldrich (Milwaukee, WI), and the cysteine-reactive probe Alexa Fluor 595 C<sub>5</sub> maleimide was purchased from Invitrogen (Madison, WI). All other reagents and chemicals were of the highest available purity. ROS membranes containing rhodopsin and  $G\beta_1\gamma_1$  were prepared as described in ref. 6.

**Protein expression and purification.**  $G\alpha_i$  and  $G\alpha_i$  HI proteins were expressed and purified as described previously<sup>6,24,38</sup> and stored at -80 °C in 50 mM Tris, 100 mM NaCl, 2 mM MgCl<sub>2</sub>, 1 mM DTT, 10  $\mu$ M GDP and 10% glycerol, pH 7.5.

**Intrinsic tryptophan fluorescence and AIF<sub>4</sub> activation.** Intrinsic tryptophan fluorescence was measured as described previously<sup>39</sup>.  $G\alpha$  (200 nM) subunits were monitored (ex/em 280:340 nm) before and after activation with 10  $\mu$ M AIF<sub>4</sub> in 50 mM Tris, 100 mM NaCl, 2 mM MgCl<sub>2</sub> and 10  $\mu$ M GDP, pH 7.5. The ability of selected  $G\alpha_i$  proteins to undergo activation-dependent changes as a result of basal nucleotide exchange of GDP for BD-GTP $\gamma$ S was measured as described previously<sup>40</sup>;  $G\alpha_i$  HI proteins exhibited a ten-times-higher rate of exchange than did wild-type proteins, owing to removal of solvent-exposed cysteine residues, as required for site-specific fluorescent labeling. Briefly, emission intensity of  $G\alpha_i$  protein (200 nM) was monitored at ex/em 280:340 nm before and after addition of GTP $\gamma$ S (10  $\mu$ M). Exchange of GDP for GTP $\gamma$ S was determined by monitoring of the relative increase of intrinsic tryptophan fluorescence, as described above. Nucleotide exchange assays were performed in buffer containing 50 mM Tris, 100 mM NaCl and 1 mM MgCl<sub>2</sub>, pH 7.5, at 18 °C. Changes in fluorescence emission were determined from at least three independent experiments. Time-dependent fluorescence changes were fit to an exponential association curve with Prism 4.0 (GraphPad Software).

**Protein labeling.**  $G\alpha_i$  HI proteins<sup>24</sup> were labeled at a concentration of approximately 1 mg/mL in buffer free of reducing agent with a 5:1 probe/protein molar ratio in 50 mM Tris, 130 mM NaCl, 2 mM MgCl<sub>2</sub> and 100  $\mu$ M GDP, pH 7.5. This was followed by quenching with  $\beta$ -mercaptoethanol and removal of unbound probe with HPLC by size exclusion with a SW2000 column (Sigma-Aldrich, St. Louis, MO). Efficiency of labeling was between 25% and 40%. Chromatography was carried out in the same buffer supplemented with 10  $\mu$ M GDP and 1 mM DTT. Monodispersity and molecular weight of the monomeric, labeled proteins was confirmed after purification by gel-filtration HPLC comparing peak retention times and peak shape to results from column calibration performed with a broad range of molecular-weight standards run on the same day as were the purified samples (Bio-Rad, Hercules, CA). The monomeric, labeled, purified proteins were pooled on the basis of their ability to undergo activation-dependent changes as measured by intrinsic Trp211 activation (described above). Proteins with mutation of Trp211 were assayed by BD-GTP $\gamma$ S binding (described below) to ensure functional integrity of the labeled proteins.

**Extrinsic fluorescence assays.** For fluorescence studies of A1-labeled proteins, the emission maxima of labeled  $G_i$  protein (400 nM) were determined by scanning emission between 590 and 750 nm, with excitation at 580 nm

after reconstitution of labeled  $G\alpha$  subunits with equimolar  $G\beta_1\gamma_1$  subunits in buffer consisting of 50 mM Tris, 100 mM NaCl, 2 mM  $MgCl_2$  and 1 mM DTT, pH 7.5, at 18 °C. All fluorescence data were analyzed as described for intrinsic tryptophan fluorescence.

A decrease in fluorescence after receptor activation indicates an increase in the polarity of the environment of the labeled residue as compared to the environment in the inactive heterotrimer. A decrease in emission upon receptor activation is consistent with a more solvent-exposed environment for the labeled residue. An increase in fluorescence is likewise correlated with a more hydrophobic environment consistent with an increase in packing for the residue upon receptor activation.

**Membrane binding assay.** Membrane binding assay was evaluated as described previously<sup>38</sup>. Briefly,  $G\alpha_i$  (5  $\mu$ M) subunits were preincubated with  $G\beta\gamma$  (10  $\mu$ M) subunits on ice for 10 min. Then, in the dark, rhodopsin (50  $\mu$ M) within ROS membranes was added to the heterotrimeric G protein in a buffer containing 50 mM Tris, pH 8.0, 100 mM NaCl and 2 mM  $MgCl_2$  and incubated on ice for 5 min. For dark measurements, reaction mixtures were protected from light for the rest of the procedure. Light-activated samples, as well as light-activated samples with GTP $\gamma$ S (100  $\mu$ M), were incubated on ice for 30 min. Membranes and supernatant were separated by centrifugation, and samples were resolved by SDS-PAGE, visualized with Coomassie blue and quantified by densitometry with a Bio-Rad Multi-Imager. The data represent the average of three independent experiments (Supplementary Fig. 6a).

**Spin labeling and DEER measurement.** Spin label (S-(1-oxy-2,2,5,5-tetramethylpyrrolidine-3-methyl)-methanethiosulfonate, 200 mM) in DMF was mixed with  $G\alpha$  subunits in a 2:1 molar ratio with buffer containing 50 mM Tris, pH 7.4, 100 mM NaCl, 2 mM  $MgCl_2$  and 50  $\mu$ M GDP. The reaction mixture was shaken gently for 16 h at 4 °C. Unreacted spin label was removed from sample by gel-filtration chromatography or extensive washing with labeling buffer by centrifugal concentrator with a molecular-mass cutoff of 10 kDa. The final labeled protein was determined by Bradford assay with bovine serum albumin as a standard. All of the spin-labeled mutants showed basal and receptor-mediated tryptophan fluorescence increases in the presence of GTP $\gamma$ S with comparable level of unlabeled  $G\alpha_i$ HI protein (Supplementary Fig. 6b). In addition to nucleotide exchange, they all showed the ability to form stable receptor–G protein complexes in the absence of G nucleotide. Double electron-electron resonance (DEER) measurements were performed on a Bruker 580 pulsed EPR spectrometer operating at Q band (33.5 GHz) with a standard four-pulse protocol<sup>41,42</sup>. Glycerol (30% w/w) was added to the samples before cooling. All experiments were carried out at 83 K. Analysis of the DEER data to determine the distance distributions,  $P(r)$ , was carried out in DeerAnalysis 2011 (ref. 43). The data were fit with Tikhonov regularization and L-curve determination of the optimal regularization parameter<sup>44</sup>

(Supplementary Fig. 7). Some data were fitted with Gaussians when the data were not adequately fitted with Tikhonov regularization. For example, there are situations in which the assumptions of Tikhonov regularization may not be suitable, as in the case of very broad distributions. These very broad distributions tend to have poorly defined L curves in the typical range used to fit most data. It is in these cases that the Gaussian distributions were used to fit the data. The parameters derived from the Gaussian–distribution overlap with the distribution obtained with Tikhonov regularization, thus omitting the uncertainty in the fine structure of the distribution. To test our assay system, we measured the distance between 90 and 238 residues before and after receptor activation, and we found comparable distance distribution with the previous study<sup>9</sup>.

31. Mandell, D.J., Coutsias, E.A. & Kortemme, T. Sub-angstrom accuracy in protein loop reconstruction by robotics-inspired conformational sampling. *Nat. Methods* **6**, 551–552 (2009).
32. Bower, M.J., Cohen, F.E. & Dunbrack, R.L. Jr. Prediction of protein side-chain rotamers from a backbone-dependent rotamer library: a new homology modeling tool. *J. Mol. Biol.* **267**, 1268–1282 (1997).
33. Bradley, P., Misura, K.M. & Baker, D. Toward high-resolution *de novo* structure prediction for small proteins. *Science* **309**, 1868–1871 (2005).
34. Choe, H.W. *et al.* Crystal structure of metarhodopsin II. *Nature* **471**, 651–655 (2011).
35. Johnston, C.A. & Siderovski, D.P. Receptor-mediated activation of heterotrimeric G-proteins: current structural insights. *Mol. Pharmacol.* **72**, 219–230 (2007).
36. Scheerer, P. *et al.* Crystal structure of opsin in its G-protein-interacting conformation. *Nature* **455**, 497–502 (2008).
37. Mchaourab, H.S., Steed, P.R. & Kazmier, K. Toward the fourth dimension of membrane protein structure: insight into dynamics from spin-labeling EPR spectroscopy. *Structure* **19**, 1549–1561 (2011).
38. Preininger, A.M. *et al.* Myristoylation exerts direct and allosteric effects on  $G\alpha$  conformation and dynamics in solution. *Biochemistry* **51**, 1911–1924 (2012).
39. Mazzoni, M.R. & Hamm, H.E. Tryptophan207 is involved in the GTP-dependent conformational switch in the  $\alpha$  subunit of the G protein transducin: chymotryptic digestion patterns of the GTP $\gamma$ S and GDP-bound forms. *J. Protein Chem.* **12**, 215–221 (1993).
40. Preininger, A.M. *et al.* Helix dipole movement and conformational variability contribute to allosteric GDP release in Gi subunits. *Biochemistry* **48**, 2630–2642 (2009).
41. Pannier, M., Veit, S., Godt, A., Jeschke, G. & Spiess, H.W. Dead-time free measurement of dipole-dipole interactions between electron spins. *J. Magn. Reson.* **142**, 331–340 (2000).
42. Zou, P. & Mchaourab, H.S. Increased sensitivity and extended range of distance measurements in spin-labeled membrane proteins: Q-band double electron-electron resonance and nanoscale bilayers. *Biophys. J.* **98**, L18–L20 (2010).
43. Jeschke, G. *et al.* DeerAnalysis2006: a comprehensive software package for analyzing pulsed ELDOR data. *Appl. Magn. Reson.* **30**, 473–498 (2006).
44. Chiang, Y.W., Borbat, P.P. & Freed, J.H. The determination of pair distance distributions by pulsed ESR using Tikhonov regularization. *J. Magn. Reson.* **172**, 279–295 (2005).